RSC Advances

PAPER

View Article Online
View Journal | View Issue

Cite this: *RSC Adv.*, 2026, **16**, 1134

Optical anisotropy induced by ultra-strong interfacial coupling in CVD-grown $WSe_2/ReSe_2$ vertical heterostructures

Yong Guo, †[a] Xiaofei Yue, †*[ab] Jiajun Chen,†[b] Qingqing Nie,[b] Chenxu Sheng,[b] Haoyu Wang,[a] Yongsheng Qin,[a] Xuechao Liu,[c] Siqi Lin,[a] Le Fang,[a] Miaosen Yang,[a] Zhijun Qiu,[b] Min Jin *[a] and Chunxiao Cong *[b]

Integrating high-mobility isotropic transition metal dichalcogenides (TMDs) with anisotropic layered materials offers an ideal strategy to break through the application bottleneck of a single material. Van der Waals assembly has proven a direct route to realize anisotropic heterostructures for polarization-sensitive electronics and photoelectronics, yet conventional methods typically rely on artificial stacking of TMD materials with varying symmetries. This approach not only limits the efficiency of fabrication but also yields poor interfacial coupling, resulting in weak anisotropy in heterostructures. Here, we directly grow high-quality monolayer WSe_2 on low-symmetry monolayer $ReSe_2$ to fabricate $WSe_2/ReSe_2$ vertical heterostructures by NaCl-assisted chemical vapor deposition (CVD). Angle-resolved polarization Raman spectroscopy confirms that the isotropic WSe_2 exhibits pronounced in-plane optical anisotropy upon combining with low-symmetry $ReSe_2$, which is attributed to the intrinsic symmetry breaking of WSe_2 induced by ultra-strong interlayer coupling between WSe_2 and $ReSe_2$. Notably, the pronounced photoluminescence (PL) quenching and shortened exciton lifetime of WSe_2 provide direct evidence of ultra-strong interfacial coupling in the CVD-grown $WSe_2/ReSe_2$ vertical heterostructures. Consequently, this study demonstrates the pivotal role of interfacial coupling in achieving high-degree anisotropy in TMD heterostructures, offering a new design paradigm for polarization-sensitive electronics and optoelectronics.

Received 24th October 2025
Accepted 10th December 2025

DOI: 10.1039/d5ra08161k

rsc.li/rsc-advances

1 Introduction

Two-dimensional (2D) van der Waals (vdW) transition metal dichalcogenides (TMDs) have attracted particular attention owing to their tunable bandgaps, excellent electronics and optoelectronic performance, and wafer-scale manufacturability.[1–4] However, most reported TMDs are high-symmetry crystals that exhibit in-plane isotropy, which fundamentally limits their prospects in applications demanding polarization-sensitive electronic and photonic responses.[5–7] At the same time, low-symmetry TMDs such as $ReSe_2$ and ReS_2 exhibit pronounced anisotropy, making them promising for polarization applications.[8,9] Nevertheless, the intrinsically modest carrier mobility and the formidable challenge of wafer-scale synthesis of these anisotropic TMDs are currently limiting their transition from laboratory demonstrations to industrial applications.[10,11]

Recently, constructing TMDs with distinct properties into heterostructures has proven an effective means to extend and modulate the intrinsic properties of individual TMDs,[12,13] advancing the development of multifunctional integrated devices. In light of this, symmetry engineering *via* vdW heterostructures is rapidly becoming a key strategy for tailoring the anisotropic properties of TMDs,[14,15] offering a practical route toward polarization-sensitive light emission and detection.[16,17] Particularly, assembling heterostructures of anisotropic and high-mobility isotropic TMDs is expected to fully exploit the performance advantage of each component.[14,18] Previous studies have shown that the anisotropic characteristics in the isotropic/anisotropic TMDs heterostructures can be both tuned and transmitted through interlayer coupling.[19,20] However, the fabrication of such isotropic/anisotropic heterostructures typically relies on the artificial stacking of different TMDs materials through dry or wet transfer methods.[17,19,20] On the one hand, these approaches inevitably introduces contaminants at the interface and may even damage the materials.[21] On the other hand, this transfer-assembled heterostructures usually exhibit poor interfacial coupling,[19,22] leading to a weak

[a]*College of Materials, Shanghai Dianji University, Shanghai 201306, China. E-mail: xf-yue@sdju.edu.cn; jmaish@aliyun.com*

[b]*School of Information Science and Technology, Fudan University, Shanghai 200433, China. E-mail: cxcong@fudan.edu.cn*

[c]*State Key Laboratory of Functional Crystals and Devices, Shanghai Institute of Ceramics, Chinese Academy of Sciences, Shanghai 200050, China*

† These authors contribute equally to this study.

anisotropy. Therefore, establishing isotropic/anisotropic TMD-based heterostructures with robust interfacial coupling is the critical first step toward unlocking TMDs for high-performance polarization-sensitive applications.

In this study, we prepare high-quality $WSe_2/ReSe_2$ vertical heterostructures in a one-step chemical vapor deposition (CVD) process, and further reveal their ultra-strong interfacial coupling through temperature-dependent and time-resolved photoluminescence (PL) spectroscopy. Angle-resolved polarization Raman spectroscopy confirms the inherent in-plane optical anisotropy of as-grown monolayer $ReSe_2$. As expected, the CVD-grown $WSe_2/ReSe_2$ vertical heterostructures exhibit pronounced optical anisotropy manifested through WSe_2 Raman modes, which stems from the symmetry breaking of WSe_2 induced by ultra-strong interfacial coupling with low-symmetry $ReSe_2$. Meanwhile, the absence of such anisotropy in the mechanically-assembled $WSe_2/ReSe_2$ heterostructure further confirms that the robust interfacial coupling is essential for symmetry engineering. Consequently, one-step-grown isotropic/anisotropic TMD-based heterostructures offer an effective strategy to polarization-sensitive optoelectronic devices. Furthermore, our findings also provide valuable insights of interfacial coupling on anisotropy engineering.

2 Experimentals

2.1 Sample fabrication and structure characterization

Monolayer $ReSe_2$ and $WSe_2/ReSe_2$ vertical heterostructures were grown through NaCl-assisted CVD method. Specifically, WO_3 power was first thermally evaporated onto a sacrificial SiO_2/Si substrate to form a uniform film of 9 nm. 50 mg Re power was dispersed in 20 ml ethanol solution, and the upper suspension was dripped onto the WO_3 film surface, followed by drying at 80 °C for 5 min. Subsequently, a single NaCl crystal (~0.01 mg) was placed on the sacrificial substrate, while a clean SiO_2/Si growth substrate was mounted face-to-face on the sacrificial substrate. This entire stack was loaded into the central heating zone of tube furnace, while Se power (200 mg) was arranged in the edge heating zone of the quartz tube. Argon (100 sccm) was continuously supplied as the carrier gas throughout the entire growth process. The central zone was heated to 935 °C and the edge zone to 240 °C over 60 min, subsequently both zones were held at their maximum temperatures for 10 min. After reaching the set temperatures, a brief 2 min H_2 (5 sccm) was introduced, and the furnace was then allowed to cool naturally to room temperature.

The surface morphology and thickness of prepared $WSe_2/ReSe_2$ vertical heterostructures were characterized using an NX10 atomic force microscope (AFM) (Park, Korea). No-contact AFM imaging was performed with an AC160TS probe (resonance frequency 270.8 kHz) in tapping mode, using an automated step-scan at 1.0 Hz with 512 × 512 pixel resolution.

2.2 Optical measurements

Raman and PL measurements were conducted using a confocal Raman microscopy system (WITec Alpha 300R) under a 532 nm laser excitation. The 1800 lines per mm and 150 lines per mm gratings were used to collect Raman and PL spectra, respectively. A 100× objective lens (Zeiss, N.A. = 0.9) was employed for room-temperature measurements. For low temperature *in situ* PL measurements, samples were mounted inside the chamber of a multifunctional system with liquid helium refrigeration (CRYO Industries of America, Inc), enabling cooling from 300 K to 10 K. Particularly, the lens was switched to a 50× long-focus objective (Zeiss, N.A. = 0.55), while the sample chamber was maintained at a high vacuum level of 10^{-3} Pa. For angle-resolved polarization Raman measurements, samples were installed at the center of a rotating platform and tuned from 0° to 180°, with a spectrum acquisition every 15° under both parallel and crossed polarization configurations.

3 Results and discussions

Fig. 1 presents the fabrication process of the $WSe_2/ReSe_2$ vertical heterostructures by space-confined CVD technique. Fig. 1a shows the schematic diagram of the CVD tube furnace, where Se precursor is placed in the left heating zone, while WO_3 and Re precursors are placed in the right heating zone. Considering the ultra-high melting point of Re (>3000 °C), a NaCl-assisted strategy was employed to achieve monolayer $ReSe_2$ growth. Fig. S1 provides the comparative optical images of $WSe_2/ReSe_2$ heterostructures grown with and without NaCl assistance. Specifically, during the CVD growth process, the introduction of NaCl auxiliaries not only lowers the reaction temperature, but also simultaneously increases the precursor supersaturation and the density of nucleation points.[23,24] Fig. 1b and c depict the growth mechanism of the $WSe_2/ReSe_2$ vertical heterostructure. When the Se and Re precursors are heated to their target temperatures, the $ReSe_2$ molecular clusters first nucleate and grow into irregular shapes on the SiO_2/Si substrate surface. Subsequently, as the WO_3 precursor reaches its set temperature, the WSe_2 molecular clusters further nucleate on the surface of the existing $ReSe_2$ and gradually grow into triangular shapes. Fig. 1d and e show the optical images of the as-grown $ReSe_2$ film and $WSe_2/ReSe_2$ heterostructures, respectively. Particularly, the successful preparation of the heterostructures combining isotropic WSe_2 with anisotropic $ReSe_2$, offering an idea platform to investigate the intrinsic anisotropic properties in vertically stacked heterostructures.

We first conducted structural and optical characterization for the vertical $WSe_2/ReSe_2$ heterostructures. Fig. S2 provides the AFM scanning images and corresponding height profiles. Here, the boundary between the underlying $ReSe_2$ and the substrate is clearly visible, while the triangular shape of the top-layer WSe_2 can also be observed. The $ReSe_2$ flake shows a thickness of approximately 1.3 nm, consistent with a monolayer characteristics on SiO_2/Si substrates. The top WSe_2 layer was scanned more precisely, exhibiting a height of approximately 0.8 nm, which is highly close to the theoretical thickness of monolayer WSe_2. These results confirm the successful formation of $WSe_2/ReSe_2$ bilayer vertical heterostructures. Furthermore, we also extracted the RMS roughness from the high-solution AFM image of the as-grown $WSe_2/ReSe_2$

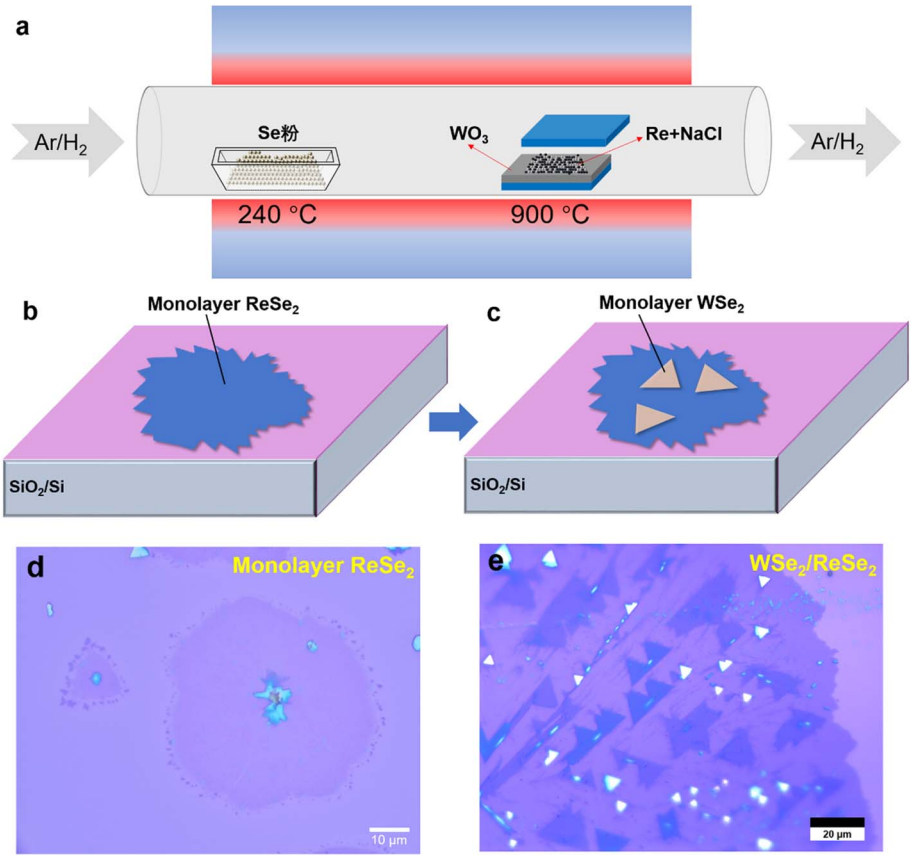

Fig. 1 Fabrication process of the $WSe_2/ReSe_2$ vertical heterostructures by NaCl-assisted CVD method. (a) The schematic diagram of the CVD tube furnace for $WSe_2/ReSe_2$ heterostructures growth. (b) and (c) The growth mechanism of the $WSe_2/ReSe_2$ vertical heterostructure. (d) Optical image of the as-grown monolayer $ReSe_2$ film. (e) Optical image of the as-grown $WSe_2/ReSe_2$ vertical heterostructures.

heterostructure, obtaining $S_q = 0.0007$ μm and $S_a = 0.0006$ μm. Such sub-nanometer roughness suggests an exceptionally flat interface. Fig. 2a shows the Raman spectrum of the monolayer $ReSe_2$ under a 532 nm laser excitation. Due to the low-symmetry crystal structure, theory predicts that there are 18 Raman modes in monolayer $ReSe_2$,[25] which is rarely observed in most transition metal dichalcogenides.[26] To obtain the accurate vibration frequency of each Raman mode, we performed detailed Lorentzian fitting for all Raman peaks, as shown by the colored dotted lines in Fig. 2a. According to the fitted results, 17 Raman modes can be successfully identified in the as-grown monolayer $ReSe_2$. Table S1 summarizes the fitted frequencies of the 17 Raman modes and compares them with the calculated values. The minute differences between experiment and theory confirm the excellent crystal quality of the as-grown monolayer $ReSe_2$. On the other hand, we also notice that only 16 Raman modes were experimentally observed in the ref. 25. This suggests that the finite spectral resolution may limit the extraction of all 18 Raman modes. Fig. 2b further compares the Raman spectra of as-grown monolayer $ReSe_2$, monolayer WSe_2, and $WSe_2/ReSe_2$ vertical heterostructure. Two prominent Raman modes E^1_{2g} (247.8 cm^{-1}) and A_{1g} (256.7 cm^{-1}) of WSe_2 are observed in the heterostructure region, which are individually assigned to the in-plane and out-of-plane vibration of W and Se atoms.[26] The inset shows a uniform Raman image of the heterostructure obtained by integrating the intensity of E^1_{2g} mode, indicating that the top-layer WSe_2 retains a pristine lattice quality. Compared with standalone monolayer WSe_2, the E^1_{2g} mode exhibits a slight redshift, whereas the A_{1g} mode undergoes a pronounced redshift in the heterostructure region. Particularly, in TMDs heterostructures, the in-plane vibration (E^1_{2g}) is known to be relatively insensitive to the interfacial interaction, while A_{1g} mode is highly sensitive to interlayer coupling due to its out-of-plane vibrational characteristic. Consequently, the marked shift of the A_{1g} peak provides compelling evidence for effective interfacial coupling within the $WSe_2/ReSe_2$ heterostructure. In addition, these weak Raman peaks originating from underlying $ReSe_2$ are observed as well, which further confirms the formation of hetero-stacked structure.

In typical bilayer TMDs heterostructures, the interaction between two components mainly depends on the interfacial coupling,[22,27] for which strong interlayer coupling is highly desired. Therefore, we further conducted PL spectroscopy measurements for the as-grown $WSe_2/ReSe_2$ heterostructures to evaluate the interlayer coupling strength, as shown in Fig. 2c. It is well known that monolayer WSe_2 exhibits strong PL emission at room temperature due to its direct bandgap feature (~1.6 eV).[28] In stark contrast, the PL emission of WSe_2 is completely

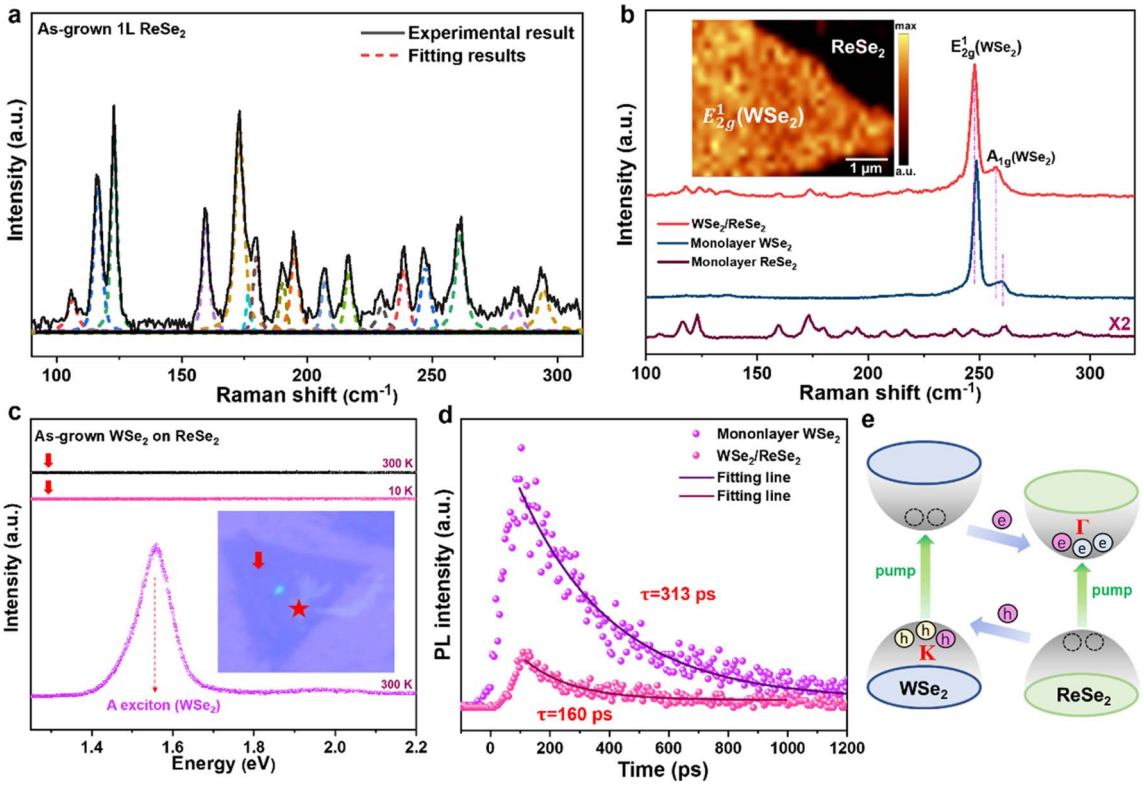

Fig. 2 Optical characterization of the CVD-grown monolayer $ReSe_2$, monolayer WSe_2, and $WSe_2/ReSe_2$ vertical heterostructures. (a) Raman spectrum of the as-grown monolayer $ReSe_2$ with detailed Lorentzian fitted peaks (colored dotted lines). (b) Comparison of Raman spectra between the monolayer $ReSe_2$, monolayer WSe_2, and $WSe_2/ReSe_2$ vertical heterostructure, the inset shows a spatial intensity map generated by integrating the E^1_{2g} peak of WSe_2. (c) PL spectra of the $WSe_2/ReSe_2$ vertical heterostructure measured at 300 K and 10 K, together with the spectrum (300 K) obtained after 1064 nm laser irradiation treatment (The red star marks the laser-irradiated region). (d) Time-resolved PL measurements of the standalone monolayer WSe_2 and $WSe_2/ReSe_2$ heterostructure. (e) The schematic diagram of interfacial charge transfer in the $WSe_2/ReSe_2$ vertical heterostructures.

quenched in the as-grown $WSe_2/ReSe_2$ heterostructures at both 300 K and 10 K, as indicated by the black and pink lines in Fig. 2c. We preliminarily attribute this pronounced quenching to two possibilities: (i) in as-grown monolayer WSe_2, a high density of defects (such as vacancies and dislocations) may act as non-radiative recombination centers, significantly reducing the radiative recombination efficiency of photo-generated carriers; (ii) ultrafast interlayer charge transfer occurs due to the type-II band alignment formed between WSe_2 and $ReSe_2$, causing significant PL quenching.[29] To verify the above deduction, we employed a 1064 nm infrared laser to perform localized heating for the CVD-grown $WSe_2/ReSe_2$ heterostructure. Through high-power irradiation, the underlying $ReSe_2$ was effectively removed (see the inset in Fig. 2c), which enables *in situ* monitoring of the WSe_2 PL emission before and after $ReSe_2$ removal. Interestingly, once the $ReSe_2$ layer is removed, the isolated monolayer WSe_2 recovers strong PL emission even at room temperature, as depicted by the purple trace. This finding strongly indicates that the as-grown monolayer WSe_2 possesses excellent lattice quality, thus ruling out the possibility that high density defects are responsible for the observed PL quenching in $WSe_2/ReSe_2$ heterostructures. Furthermore, we also provided more direct experimental evidence, as depicted in Fig. 2d. We conducted time-resolved PL measurements to compare the A-exciton lifetime of WSe_2 in the heterostructure with that of the standalone monolayer WSe_2. According to the fitting results, the A-exciton of monolayer WSe_2 exhibits a lifetime of ~313 ps, whereas the lifetime is reduced to ~160 ps in the heterostructure region. This pronounced shortening provides direct evidence of efficient interlayer charge transfer at the $WSe_2/ReSe_2$ interface.

Consequently, we can reasonably conclude that the PL quenching behavior occurred in $WSe_2/ReSe_2$ heterostructures originates from high-efficiency interlayer charge transfer.[29,30] As illustrated in Fig. 2e, upon 532 nm laser excitation, the photo-generated electrons are first excited to the conduction band minimum (CBM) of WSe_2, and subsequently transfer to the CBM of $ReSe_2$ in an extremely short time scale. Simultaneously, the photo-generated holes transfer from the valence band maximum (VBM) of $ReSe_2$ to that of WSe_2, leading to electron–hole separation across the two layers. Notably, such efficient interfacial charge transfer usually necessitates strong interlayer coupling between the constituent layers of heterostructures.[22,31] The experimental findings collectively support the conclusion that the as-grown $WSe_2/ReSe_2$ heterostructures possess robust interfacial coupling strength.

It should be noted that in most cases the PL quenching induced by interlayer charge transfer is incomplete, intralayer exciton emission from the constituent layers can still be detected at low temperatures.[32,33] In this present study, however, no intralayer exciton signal from WSe_2 is observed even at 10 K, providing further evidence for exceptionally strong interfacial coupling. In addition, the absence of interlayer exciton emission at low temperature is mainly ascribed to momentum mismatch.[34] Specifically,in the $WSe_2/ReSe_2$ heterostructure, interlayer exciton emission originates from the recombination of electrons at CBM of $ReSe_2$ and holes at VBM of WSe_2. Theoretical studies show that the CBM of monolayer $ReSe_2$ is located at the Γ point of the Brillouin zone,[35] whereas the VBM of monolayer WSe_2 lies at the K point.[36] This momentum-space mismatch greatly suppresses the probability of radiative recombination between spatially separated electrons and holes.[34]

As is well known, monolayer WSe_2 is intrinsically intralayer isotropic, whereas monolayer $ReSe_2$ is a typical intralayer anisotropic material. The strong interlayer coupling demonstrated here in the CVD-grown $WSe_2/ReSe_2$ heterostructures therefore provides an ideal platform for probing how $ReSe_2$ anisotropy modulates WSe_2 properties. Fig. S3a presents the polarized Raman spectra of the monolayer $ReSe_2$ collected in both parallel (*XX*) and crossed (*XY*) configurations. Notice that some Raman modes exhibit pronounced intensity difference in two configurations. This is due to the Raman intensity being determined by the Raman tensors of vibration modes and the incident and scattered light polarization vectors.[37,38] Particularly, each $ReSe_2$ vibration mode possesses a definite symmetry that dictates its Raman tensor non-zero elements, while the contribution of these elements to the scattered intensity is selectively weighted by the polarization configurations.[37,38] Fig. S3b shows the polarized Raman spectra of the $WSe_2/ReSe_2$ heterostructure recorded in two configurations. Clearly, two vibration modes of WSe_2 exhibit distinct polarization responses: the E^1_{2g} intensity drops markedly in the crossed configuration, whereas A_{1g} intensity remains almost unchanged.

Moreover, we performed the angle-resolved polarization Raman measurements of the monolayer $ReSe_2$. The sample is rotated from 0° to 180°, with a spectrum acquisition every 15° in both parallel and crossed configurations. The evolution of the polarized Raman spectra (*XX*) of the monolayer $ReSe_2$ is shown in Fig. 3a, while the corresponding intensity color map is provided in Fig. 3b for better visualization of the angle dependence of each phonon mode. For *XX* configuration, the frequencies of various Raman modes in monolayer $ReSe_2$ exhibit little change with angles, whereas their intensities present pronounced angle dependence, demonstrating the high in-plane anisotropy of our as-grown monolayer $ReSe_2$. To quantitatively characterize the anisotropy characteristic of $ReSe_2$, we preformed detailed lorentzian fitting for the angle-resolved polarized Raman spectra to extract the intensity of each mode. Considering the 17 observed Raman-active modes are all first-order A_g symmetry, we primarily focused on two prominent peaks at 123 cm^{-1} and 173 cm^{-1}. The normalized intensities of the two modes as a function of rotation angle are presented in the polar diagrams of Fig. 3c and d, respectively. Clearly, the intensities of the $ReSe_2$ Raman modes at 123 cm^{-1} and 173 cm^{-1} vary periodically with rotation angle, with a period close to 90°. Owing to the different basis functions of the C_i point group, not all Raman modes exhibit a 90° period,[39] for example, the 261 cm^{-1} mode shows a ~180° periodicity (see Fig. 3b). In addition, Fig. S4 presents the angle-resolved Raman responses of the as-grown monolayer $ReSe_2$ under *XY* polarization configuration. Similarly, the intensities of the 123 cm^{-1} and 173 cm^{-1} Raman modes exhibit significant angle dependence, which further indicates the strong in-plane anisotropy of monolayer $ReSe_2$.

Fig. 3e displays the evolution of the polarized Raman spectra (*XX* configuration) of the as-grown monolayer WSe_2, while the corresponding intensity color map is provided in Fig. 3f. The normalized intensities of the E^1_{2g} and A_{1g} modes *versus* rotation angle are plotted in the polar diagrams of Fig. 3g and h. As expected, no obvious periodic variation is observed, consistent with the isotropic nature of monolayer WSe_2. Based on the preceding evidence for ultra-strong interlayer coupling in our CVD-grown $WSe_2/ReSe_2$ heterostructures, we anticipate that the pronounced in-plane anisotropy of $ReSe_2$ may induce a measurable anisotropy in the top-layer WSe_2. To verify the deduction, we further conducted angle-resolved polarization Raman measurements of the as-grown $WSe_2/ReSe_2$ heterostructures. Fig. 3i presents the angle-resolved polarized Raman spectra of the $WSe_2/ReSe_2$ heterostructure under parallel configuration, with the corresponding intensity color map shown in Fig. 3j. The WSe_2 E^1_{2g} mode exhibits a pronounced period intensity modulation, whereas the A_{1g} signal is too weak for its periodicity to be directly observed. Likewise, lorentzian fitting was employed to extract the angle-dependent intensities of E^1_{2g} and A_{1g} modes, whose normalized results are displayed in the polar diagrams of Fig. 3k and l, respectively. Interestingly, the two Raman modes of WSe_2 exhibit a consistent ~90° period, while the E^1_{2g} mode demonstrates a stronger angle dependence relative to the A_{1g} mode. Particularly, E^1_{2g} mode typically involves in-plane vibrations of W and Se atoms, making it more sensitive to in-plane symmetry variations than A_{1g} mode.[26] These experimental findings clearly suggest that the Raman modes of top-layer WSe_2 exhibit optical in-plane anisotropy in our CVD-grown $WSe_2/ReSe_2$ heterostructures, evidencing a lattice-symmetry perturbation induced within WSe_2 layer. We attribute this transformation to the strong interfacial coupling between WSe_2 and low-symmetry $ReSe_2$ substrate, which induces a pronounced anisotropic phonon-photon coupling behavior in the WSe_2 layer.

Specifically, monolayer WSe_2 is intrinsically in-plane isotropic, whereas its phonon scattering exhibits pronounced angle dependence (*XX*) as bonding with $ReSe_2$ *via* van der Waals forces. Such polarization-sensitive Raman scattering usually signals a modification of in-plane rotational symmetry.[14,15] In other word, the ultra-strong interlayer coupling between monolayer WSe_2 and low-symmetry $ReSe_2$ breaks the intrinsic symmetry of WSe_2. Meanwhile, such strong interlayer coupling allows $ReSe_2$ to impose an anisotropic potential on WSe_2,

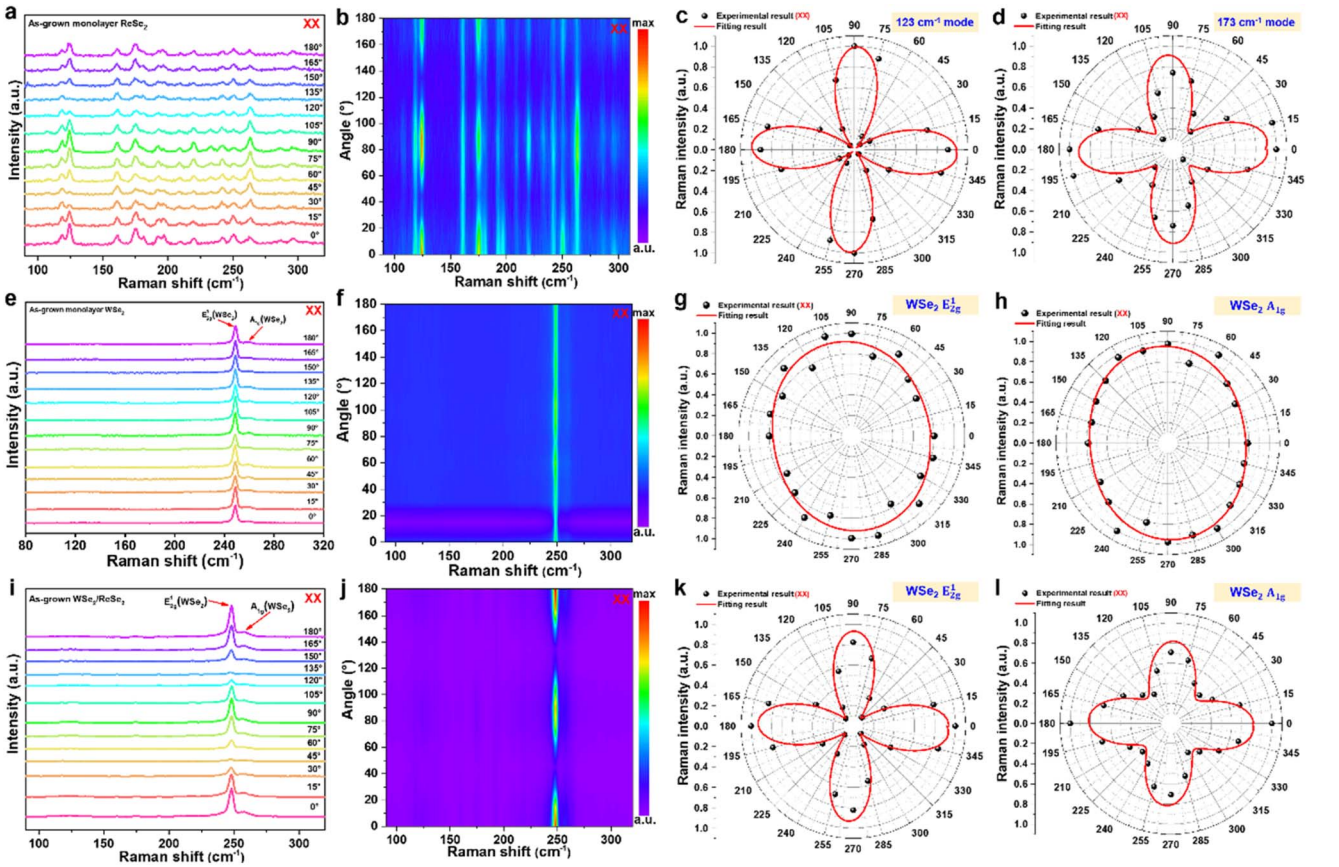

Fig. 3 Polarization Raman measurements of the CVD-grown monolayer $ReSe_2$, monolayer WSe_2, and $WSe_2/ReSe_2$ vertical heterostructure. (a) Angle-resolved polarized Raman spectra of the as-grown monolayer $ReSe_2$ under parallel configuration. (b) The Raman intensity color map corresponding to (a). (c) and (d) The normalized Raman intensities of $ReSe_2$ 123 cm^{-1} and 173 cm^{-1} modes as a function of rotation angle. (e) Angle-resolved polarized Raman spectra of the as-grown monolayer WSe_2 under parallel configuration. (f) The Raman intensity color map corresponding to (e). (g) and (h) The normalized Raman intensities of WSe_2 E^1_{2g} and A_{1g} modes as a function of rotation angle. (i) Angle-resolved polarized Raman spectra of the as-grown $WSe_2/ReSe_2$ vertical heterostructure under parallel configuration. (j) The Raman intensity color map corresponding to (i). (k) and (l) In $WSe_2/ReSe_2$ heterostructure, the normalized Raman intensities of WSe_2 E^1_{2g} and A_{1g} modes as a function of rotation angle.

driving its phonon scattering to become in-plane anisotropic. Moreover, the charge redistribution and band renormalization induced by efficient interlayer charge transfer may further produce a contribution to the anisotropy of phonon–photon coupling behavior.[40] Particularly, Fig. S5 presents the angle-resolved polarized Raman spectra of the $WSe_2/ReSe_2$ heterostructure under *XY* configuration. In contrast to *XX* configuration, both Raman modes of WSe_2 exhibit weak angle dependence, with a period intensity modulation of ~180°, which implies that the anisotropy induced by strong interlayer coupling also follows the Raman tensor selection rule.

To further verify this conclusion, we fabricated an additional vertical $WSe_2/ReSe_2$ heterostructure through transferring a mechanically exfoliated (ME) monolayer WSe_2 onto the as-grown monolayer $ReSe_2$. Fig. 4a presents the optical image of the sample, where the yellow frame represents the heterostructure region. We respectively acquired the Raman spectra in the individual $ReSe_2$, WSe_2 and $WSe_2/ReSe_2$ heterostructure regions, as shown in Fig. 4b. In the heterostructure, both Raman peaks of WSe_2 are clearly visible, whereas the $ReSe_2$ peaks are too weak to be observed, consistent with the CVD-grown samples (see Fig. 2b). In contrast to the pronounced redshift observed in CVD-grown heterostructures, the unchanged peak position of WSe_2 indicates a relatively weak interfacial coupling in the ME $WSe_2/ReSe_2$ heterostructure. Fig. 4c directly compares the PL spectrum of monolayer WSe_2 on SiO_2/Si substrate with that of the ME $WSe_2/ReSe_2$ heterostructure at room temperature. Note that, the mechanically-assembled heterostructure sample had been annealed at 300 °C for 4 hours to strengthen interfacial coupling before optical measurements. As expected, the WSe_2 PL emission is incompletely quenched in the heterostructure, with a weak emission peak still visible (red curve). This incomplete PL quenching at room temperature suggests a relative weak interlayer coupling in the mechanically-assembled $WSe_2/ReSe_2$ heterostructure compared to that of the CVD-grown sample. Therefore, we further conducted angle-resolved polarization Raman measurements for the individual WSe_2 and ME $WSe_2/ReSe_2$ heterostructure, respectively. Fig. 4d–g display the intensity color maps of the angle-resolved Raman spectra for the

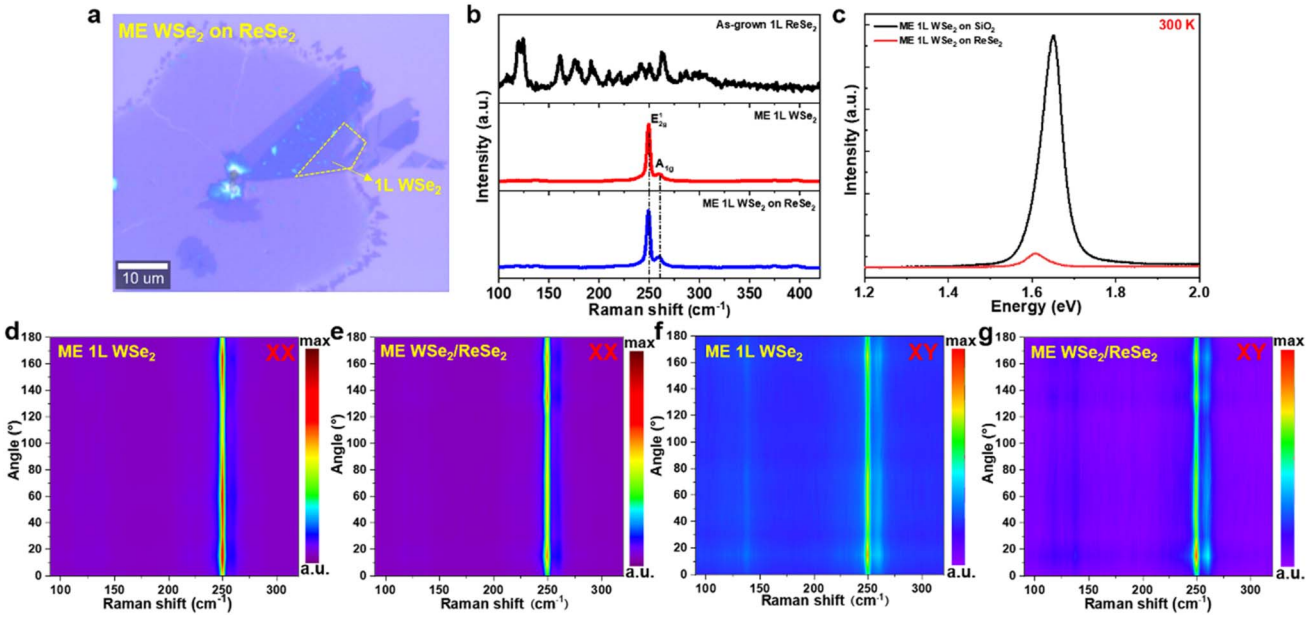

Fig. 4 Optical anisotropy characterization of the mechanically-assembled $WSe_2/ReSe_2$ heterostructure. (a) Optical image of the mechanically-assembled $WSe_2/ReSe_2$ heterostructure. (b) Raman spectra measured in the individual $ReSe_2$, WSe_2 and $WSe_2/ReSe_2$ heterostructure regions. (c) Comparison of the PL spectra between the monolayer WSe_2 and ME $WSe_2/ReSe_2$ heterostructure. (d) and (e) Raman intensity color maps of the monolayer WSe_2 and ME $WSe_2/ReSe_2$ heterostructure under parallel configuration. (f) and (g) Raman intensity color maps of the monolayer WSe_2 and ME $WSe_2/ReSe_2$ heterostructure under crossed configuration.

monolayer WSe_2 and ME $WSe_2/ReSe_2$ heterostructure, recorded in both *XX* and *XY* polarization configurations. Intuitively, the WSe_2 Raman modes in the ME $WSe_2/ReSe_2$ heterostructure remain angle-independent, and their intensity evolution almost keep completely consistent with that of monolayer WSe_2 on SiO_2/Si. These experimental results indicate that there is no in-plane anisotropy is induced in the WSe_2 layer owing to the weak interlayer coupling in the mechanically-assembled $WSe_2/ReSe_2$ heterostructure. This finding further corroborates that the pronounced in-plane anisotropy of WSe_2 in CVD-grown $WSe_2/ReSe_2$ heterostructures stems from robust interlayer coupling.

4 Conclusions

In summary, high-quality $WSe_2/ReSe_2$ vertical heterostructures are grown by one-step CVD technique and exhibit ultra-strong interfacial coupling, evidenced by complete WSe_2 PL quenching. Angle-resolved polarized Raman spectroscopy reveals that the Raman modes of WSe_2 exhibit obvious in-plane anisotropy in CVD-grown $WSe_2/ReSe_2$ vertical heterostructures. This is attributed to the intrinsic symmetry breaking of WSe_2 induced by strong interlayer coupling between WSe_2 and low-symmetry $ReSe_2$. Our results clarify how interfacial coupling affects anisotropy across van der Waals interfaces and provide a foundation for designing polarization-sensitive optoelectronic devices based on anisotropic TMDs heterostructures.

Author contributions

Chunxiao Cong, Min Jin and Xiaofei Yue directed the research work. Yong Guo, Xiaofei Yue and Jiajun Chen conceived and designed the experiments. Jiajun Chen fabricated the samples. Yong Guo and Xiaofei Yue conducted the experiments and analyzed the data. Yong Guo and Xiaofei Yue co-wrote the manuscript. All authors discussed the results and commented on the manuscript.

Conflicts of interest

There are no conflicts to declare.

Data availability

The data supporting this article have been included as part of the supplementary information (SI). Supplementary information: growth situation with/without NaCl, AFM height profiles, and *XY*-polarization Raman results. See DOI: https://doi.org/10.1039/d5ra08161k.

Acknowledgements

This work is supported by the National Natural Science Foundation of China (62374037, 52371193, 52272006), the Chenguang Program supported by the Shanghai Education Development Foundation & Shanghai Municipal Education Commission, the Shanghai Shuguang Program, the Shanghai Academic Research Leader (23XD1421200), the Shanghai

Rising-Star Program (23QA1403900), the Program for Professor of Special Appointment (Eastern Scholar) at Shanghai Institutions (TP2022122), the Shanghai Oriental Talented Youth Project, Space Application System of China Manned Space Program (KJZYY-NCL-0405), Zhejiang Provincial Natural Science Foundation of China (No. LD25E020001), Opening Project of State Key Laboratory of Functional Crystals and Devices (SKLFCD202505SIC).

Notes and references

1 X. Zhang, Z. C. Lai, Q. L. Ma and H. Zhang, *Chem. Soc. Rev.*, 2018, **47**, 3301–3338.
2 Y. Wang, S. Sarkar, H. Yan and M. Chhowalla, *Nat. Electron.*, 2024, **7**, 638–645.
3 J. H. Wang, X. Z. Xu, T. Cheng, L. H. Gu, R. X. Qiao, Z. H. Liang, D. D. Ding, H. Hong, P. M. Zheng, Z. B. Zhang, Z. H. Zhang, S. Zhang, G. L. Cui, C. Chang, C. Huang, J. J. Qi, J. Liang, C. Liu, Y. G. Zuo, G. D. Xue, X. J. Fang, J. P. Tian, M. H. Wu, Y. Guo, Z. X. Yao, Q. Z. Jiao, L. Liu, P. Gao, Q. Y. Li, R. Yang, G. Y. Zhang, Z. L. Tang, D. P. Yu, E. G. Wang, J. M. Lu, Y. Zhao, S. W. Wu, F. Ding and K. H. Liu, *Nat. Nanotech.*, 2022, **17**, 33–38.
4 S. Ghosh, A. Varghese, K. Thakar, S. Dhara and S. Lodha, *Nat. Commun.*, 2021, **12**, 3336.
5 M. Koperski, M. R. Molas, A. Arora, K. Nogajewski, A. O. Slobodeniuk, C. Faugeras and M. Potemski, *Nanophotonics*, 2017, **6**, 1289–1308.
6 X. Hu, L. Yan, L. Y. Ding, N. N. Zheng, D. Li, T. Ji, N. D. Chen and J. Q. Hu, *Coordin. Chem. Rev.*, 2024, **499**, 215504.
7 S. Joseph, J. Mohan, S. Lakshmy, S. Thomas, B. Chakraborty, S. Thomas and N. Kalarikkal, *Mater. Chem. Phys.*, 2023, **297**, 127332.
8 Y. C. Lin, H. P. Komsa, C. H. Yeh, T. Björkman, Z. Y. Liang, C. H. Ho, Y. S. Huang, P. W. Chiu, A. V. Krasheninnikov and K. Suenaga, *ACS Nano*, 2015, **9**, 11249–11257.
9 S. X. Yang, C. Wang, H. Sahin, H. Chen, Y. Li, S. S. Li, A. Suslu, F. M. Peeters, Q. Liu, J. B. Li and S. Tongay, *Nano Lett.*, 2015, **15**, 1660–1666.
10 E. F. Liu, Y. J. Fu, Y. J. Wang, Y. Q. Feng, H. M. Liu, X. G. Wan, W. Zhou, B. G. Wang, L. B. Shao, C. H. Ho, Y. S. Huang, Z. Y. Cao, L. G. Wang, A. D. Li, J. W. Zeng, F. Q. Song, X. R. Wang, Y. Shi, H. T. Yuan, H. Y. Hwang, Y. Cui, F. Miao and D. Y. Xing, *Nat. Commun.*, 2015, **6**, 6991.
11 F. F. Cui, X. B. Li, Q. L. Feng, J. B. Yin, L. Zhou, D. Y. Liu, K. Q. Liu, X. X. He, X. Liang, S. Z. Liu, Z. B. Lei, Z. H. Liu, H. L. Peng, J. Zhang, J. Kong and H. Xu, *Nano Res.*, 2017, **10**, 2732–2742.
12 R. X. Wu, H. M. Zhang, H. F. Ma, B. Zhao, W. Li, Y. Chen, J. T. Liu, J. Y. Liang, Q. Y. Qin, W. X. Qi, L. Chen, J. Li, B. Li and X. D. Duan, *Chem. Rev.*, 2024, **124**, 10112–10191.
13 M. M. Liu, S. H. Li, Y. K. Guo, L. Q. Zhang, D. Y. Shen, Q. Ye, Z. F. Peng, W. X. Qi, R. X. Wu, J. Li and X. D. Duan, *Adv. Funct. Mater.*, 2025, **35**, 2500876.
14 Z. Y. Li, J. W. Huang, L. Zhou, Z. Xu, F. Qin, P. Chen, X. J. Sun, G. Liu, C. Q. Sui, C. Y. Qiu, Y. F. Lu, H. Y. Gou, X. X. Xi, T. Ideue, P. Z. Tang, Y. Iwasa and H. T. Yuan, *Nat. Commun.*, 2023, **14**, 5568.
15 X. Xie, J. N. Ding, B. Wu, H. H. Zheng, S. F. Li, J. He, Z. W. Liu, J. T. Wang and Y. P. Liu, *Appl. Phys. Lett.*, 2023, **123**, 222101.
16 L. Ye, P. Wang, W. J. Luo, F. Gong, L. Liao, T. D. Liu, L. Tong, J. F. Zang, J. B. Xu and W. D. Hu, *Nano Energy*, 2017, **37**, 53–60.
17 S. W. Zhao, J. C. Wu, K. Jin, H. Y. Ding, T. S. Li, C. Z. Wu, N. Pan and X. P. Wang, *Adv. Funct. Mater.*, 2018, **28**, 1802011.
18 A. Usman, M. A. Aly, H. Masenda, J. J. P. Thompson, S. M. Gunasekera, M. Mucha-Kruczynski, S. Brem, E. Malic and M. Koch, *Nanoscale*, 2022, **14**, 10851–10861.
19 M. Zhao, W. T. Zhang, M. M. Liu, C. Zou, K. Q. Yang, Y. Yang, Y. Q. Dong, L. J. Zhang and S. M. Huang, *Nano Res.*, 2016, **9**, 3772–3780.
20 B. Wu, X. Xie, H. H. Zheng, S. F. Li, J. N. Ding, J. He, Z. W. Liu and Y. P. Liu, *Opt. Lett.*, 2023, **48**, 5867–5870.
21 X. F. Yue, J. J. Chen, J. K. Han, Y. B. Shan, S. W. Shen, W. X. Wu, B. J. Liu, L. J. Li, Y. Chen, R. J. Zhang, L. G. Hu, R. Liu, Z. J. Qiu and C. X. Cong, *Sci. China Mater.*, 2024, **67**, 3012–3020.
22 Y. B. Shan, X. F. Yue, J. J. Chen, B. G. M. Ekoya, J. K. Han, L. G. Hu, R. Liu, Z. J. Qiu and C. X. Cong, *ACS Appl. Nano Mater.*, 2022, **5**, 17986–17994.
23 M. Suleman, S. H. Lee, M. Kim, V. Nguyen, M. Riaz, N. Nasir, S. Kumar, H. M. Park, J. W. Jung and Y. Seo, *ACS Omega*, 2022, **7**, 30074–30086.
24 A. Singh, M. Moun, M. Sharma, A. Barman, A. K. Kapoor and R. Singh, *Appl. Surf. Sci.*, 2021, **538**, 148201.
25 D. Wolverson, S. Crampin, A. S. Kazemi, A. Ilie and S. J. Bending, *ACS Nano*, 2014, **8**, 11154–11164.
26 X. Zhang, X. F. Qiao, W. Shi, J. B. Wu, D. S. Jiang and P. H. Tan, *Chem. Soc. Rev.*, 2015, **44**, 2757–2785.
27 W. W. Li, Z. Q. Yang, M. T. Sun and J. Dong, *Rev. Phys.*, 2022, **9**, 100077.
28 T. F. Yan, X. F. Qiao, X. N. Liu, P. H. Tan and X. H. Zhang, *Appl. Phys. Lett.*, 2014, **105**, 101901.
29 X. X. Han, D. W. He, L. Zhang, S. C. Hao, S. Y. Liu, J. L. Fu, Q. Miao, J. Q. He, Y. S. Wang and H. Zhao, *J. Mater. Res.*, 2020, **35**, 1417–1423.
30 L. Zhang, D. W. He, J. Q. He, Y. Fu, A. Bian, X. X. Han, S. Y. Liu, Y. S. Wang and H. Zhao, *Opt. Express*, 2019, **27**, 17851–17858.
31 P. Zereshki, P. Yao, D. W. He, Y. S. Wang and H. Zhao, *Phys. Rev. B*, 2019, **99**, 195438.
32 H. Liu, Y. X. Zong, P. Wang, H. Y. Wen, H. B. Wu, J. B. Xia and Z. M. Wei, *J. Phys. D: Appl. Phys.*, 2021, **54**, 053001.
33 S. H. Chen, Z. J. Sun, H. Liu, H. W. Xu, C. Wang, R. Han, Z. H. Wang, S. C. Huang, X. L. Zhao, Z. K. Chen, W. Z. Li and D. M. Liu, *Nanoscale*, 2024, **16**, 14089–14095.
34 J. J. Chen, X. F. Yue, Y. B. Shan, H. S. Wang, J. K. Han, H. M. Wang, C. X. Sheng, L. G. Hu, R. Liu, W. H. Yang, Z. J. Qiu and C. X. Cong, *RSC Adv.*, 2023, **13**, 18099–18107.
35 J. Q. Zong, W. X. Ji, P. Li and P. J. Wang, *Mater. Res. Express*, 2020, **7**, 055018.

36 Q. H. Wang, K. Kalantar-Zadeh, A. Kis, J. N. Coleman and M. S. Strano, *Nat. Nanotech.*, 2012, **7**, 699–712.
37 M. A. Pimenta, G. C. Resende, H. B. Ribeiro and B. R. Carvalho, *Phys. Chem. Chem. Phys.*, 2021, **23**, 27103–27123.
38 G. C. Resende, G. A. S. Ribeiro, O. J. Silveira, J. S. Lemos, J. C. Brant, D. Rhodes, L. Balicas, M. Terrones, M. S. C. Mazzoni, C. Fantini, B. R. Carvalho and M. A. Pimenta, *2D Mater.*, 2021, **8**, 025002.
39 Y. Choi, K. Kim, S. Y. Lim, J. Kim, J. M. Park, J. H. Kim, Z. Lee and H. Cheong, *Nanoscale Horiz.*, 2020, **5**, 308–315.
40 I. Sánchez-Ramírez, M. G. Vergniory and F. de Juan, *Phys. Rev. B*, 2024, **110**, 195138.